

Journal of Materials Chemistry C

Materials for optical, magnetic and electronic devices

Accepted Manuscript

This article can be cited before page numbers have been issued, to do this please use: M. Dommett, M. Rivera, M. T. H. Smith and R. Crespo-Otero, *J. Mater. Chem. C*, 2020, DOI: 10.1039/C9TC05717J.



This is an Accepted Manuscript, which has been through the Royal Society of Chemistry peer review process and has been accepted for publication.

Accepted Manuscripts are published online shortly after acceptance, before technical editing, formatting and proof reading. Using this free service, authors can make their results available to the community, in citable form, before we publish the edited article. We will replace this Accepted Manuscript with the edited and formatted Advance Article as soon as it is available.

You can find more information about Accepted Manuscripts in the [Information for Authors](#).

Please note that technical editing may introduce minor changes to the text and/or graphics, which may alter content. The journal's standard [Terms & Conditions](#) and the [Ethical guidelines](#) still apply. In no event shall the Royal Society of Chemistry be held responsible for any errors or omissions in this Accepted Manuscript or any consequences arising from the use of any information it contains.

Cite this: DOI: 10.1039/xxxxxxxxxx

Molecular and Crystalline Requirements for Solid State Fluorescence Exploiting Excited State Intramolecular Proton Transfer †

Michael Dommett, Miguel Rivera, Matthew T. H. Smith, and Rachel Crespo-Otero*^a

Received Date

Accepted Date

DOI: 10.1039/xxxxxxxxxx

www.rsc.org/journalname

Aggregation induced emission offers a route to the development of emissive technologies based on solely organic systems. However, maximising fluorescence quantum efficiencies (QE) is a formidable challenge in attaining first-principles materials design, due to the interplay between the electronic structure of the chromophore and the morphology of the material. The identification of radiative and nonradiative channels, and how these are affected by aggregation, can rationalise emissive properties and aid in the design of yet more efficient fluorophores in the condensed phase. In the current work, we examine the mechanism behind the solid state luminescence enhancement in two related families of compounds with lasing properties, which undergo excited state intramolecular proton transfer (ESIPT). We systematically investigate competing excited state decay channels in a total of eleven crystals to evaluate the factors needed for efficient ESIPT fluorophores, aided by a full evaluation of the crystal structures, exciton coupling, and exciton hopping rates. We show that in addition to the restriction of non-radiative pathways, an efficient ESIPT is essential to maximise the QE in the solid state. This extensive study of structure-property relationships for fluorophores based on the ESIPT mechanism bridges the understanding of molecular photophysics with crystal structure, accelerating the development of highly efficient solid state emitters.

1 Introduction

Luminescent organic materials have technological promise for applications such as light-emitting diodes, field effect transistors, imaging and detection, and solid state lasers.^{1–7} Molecular organic systems offer the opportunity to tune absorption and emission characteristics for a desired application, through chromophore modification and crystal engineering. However, such control, at least from a design point of view, remains challenging due to the complex structure-property relationships in the condensed phase.

Optimising luminescence quantum efficiencies (QE) is

imperative to making such devices and materials viable for use. This can require complex and laborious substituent modification to inhibit nonradiative decay, in particular, due to the difficulties in controlling 3D molecular arrangements. Aggregation caused quenching (ACQ) has traditionally been the first obstacle to overcome in this process, since fluorescence quenching is highly common in conjugated aromatic systems as $\pi\pi$ interactions arise in the solid state. In past years researchers have developed a strategy to overcome ACQ *via* aggregation induced emission (AIE), where fluorescence is turned on upon molecular aggregation.^{8,9}

Numerous mechanisms have been proposed to account for AIE, due to the variety of reported systems, including J-aggregate formation, suppression of Kasha's rule of fluorescence, excimer formation, restriction of intramolecular motions (RIM), and restricted access to conical intersec-

^a School of Biological and Chemical Sciences, Materials Research Institute, Queen Mary University of London, Mile End Road, London E1 4NS, UK;

E-mail: r.crespo-otero@qmul.ac.uk

† Electronic Supplementary Information (ESI) available: [details of any supplementary information available should be included here]. See DOI: 10.1039/b000000x/

tions (RACI).^{7,10–16} Theoretical investigation into the AIE mechanism has been led by the groups of Peng and Shuai, who have developed formalism based on the Fermi Golden Rule approach to calculate radiative and nonradiative decay rates in AIE systems.^{17–23} The work of Blancafort *et al.* has shown that S_1 - S_0 conical intersections (CIs) also play a role in the solid state.^{15,16} These theoretical frameworks have enabled researchers to understand the emitting properties of a myriad of systems.²⁴

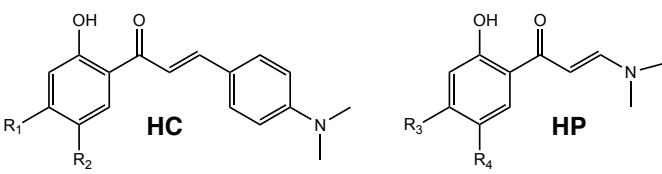
As well as the electronic properties of the chromophore, intermolecular interactions become photophysically important in the solid state due to the dense packing in organic crystals. To describe the enhancement of emission in the solid state and highlight the synergy between intramolecular and intermolecular interactions, Gierschner *et al.*²⁵ have suggested the use of the term solid state luminescence enhancement (SLE) that can be applied to solid solutions, amorphous, polycrystalline or single-crystalline materials. In this paper, we analyse a set of single crystals which display SLE.

Since the excited state is often localised on just a few molecular units, the effect of interactions among the molecules is commonly examined through Kasha's exciton theory.^{7,10,25–27} Based on this model, dimers are generally assigned as H-aggregates based on the Coulomb interaction of transition dipole moments aligning side-by-side, whilst J-aggregates arise when a slip in the x -plane (long axis) occurs. At small intermolecular distances however, the sole use of the Coulomb interaction neglects the important contribution of short-range coupling effects, resulting in interferences which cannot be described by an electrostatic interpretation alone.²⁷ Furthermore, when there is considerable perturbation between the Franck-Condon and the equilibrated excited state, Kasha's interpretation of H- and J-aggregates is less clear.

In this work we examine the electronic properties of the chromophore, the intermolecular relationships in the molecular crystal, and the crystal structure, to rationalise the observed fluorescence behaviour for a set of related organic materials undergoing excited state intramolecular proton transfer (ESIPT). ESIPT involves a four level photocycle between enol (E) and keto (K) tautomers triggered by electronic excitation in the E form. ESIPT followed by emission from the resultant K^* minimum (on the excited state PES) affords a large Stokes shift, separating the absorption and emission bands. Competition between E^* and K^* emission can be tuned, for example, through substituent modification and choice of solvent.^{28–33}

Chalcone-based compounds, comprising an aromatic ketone and enone system, have found application in both technological and biological settings.^{33–48} The lasing prop-

Table 1 Molecular structures and QEs (Φ) in the solid state (single crystals)^{49–51}



	R ₁	R ₂	Φ		R ₃	R ₄	Φ
HC1	H	H	0.32	HP1	H	H	0.74
HC2	CH ₃	H	0.25	HP2	F	H	0.84
HC3	OCH ₃	CH ₃	0.26	HP3	OCH ₃	H	0.77
HC4	H	CH ₃	<0.01	HP4	H	F	0.72
HC5	H	OCH ₃	<0.01				
HC6	F	H	0.41				
HC7	H	F	0.10				

erties of ESIPT emitters based on chalcone skeletons has aroused attention recently. In this work we investigate the properties of 2'-hydroxchalcone (**HC**) derivatives, and their mono-aryl analogues based on 2-hydroxyphenylpropenone (**HP**). The systems and properties are summarised in Table 1.^{49–51} All reported quantum yields were obtained for single crystals, consequently the effect of trapping as a source of loss of efficiency can be ruled out.¹⁰

The crystal packing, absorption and emission wavelength, and crucially the QE, are all dependent on the choice of substituent and number of aromatic rings. For structures based on **HC**, emission is dependent on the choice of substituent, which indirectly affects the packing mode.⁴⁹ Previous theoretical investigations show that fluorescence is witnessed when the conical intersection is energetically inaccessible in the solid state. Furthermore, localisation of the excited state onto one molecule in the crystal promotes the crucial ESIPT step.^{52,53}

Closely related to **HC** are the family of **HP** derivatives.⁵⁰ In contrast to **HC**, and other organic fluorophores, **HP** compounds contain only a single aryl group and have remarkable QEs, ranging from 0.72–0.84. This has been qualitatively attributed in experimental studies to the herringbone packing mode and molecular rigidity reducing non-radiative decay. Theoretical investigation can offer insight into the factors which confer this increase in QE, enabling further understanding into how to maximise fluorescence from first principles.

Herein we investigate the factors which mediate the increased fluorescence activity for **HP** compared to **HC** systems with particular focus on the role of the crystal structure and exciton couplings. Based on our previous work, we analyse the three step mechanism to enhance radiative decay in ESIPT solid state emitters; I) localisation of

excited state to one monomer, II) bias for K^* decay over E^* , III) an energetically inaccessible conical intersection.⁵³ We use quantum chemical and hybrid simulations to address each of these steps to show how the **HP** systems have an increased potency in each one with respect to their **HC** counterparts, resulting in the **HP** systems' increased fluorescence in the solid state.

2 Results and Discussion

2.1 Crystal morphology

Excited state mechanisms in the solid state are controlled by intermolecular interactions, where the crystal structure determines the free volume available for the relaxation of the chromophore in the excited state. We begin by analysing the crystal structures of the eleven compounds. Each crystal can be examined initially from the perspective of a monomeric chromophore. To this end, we use Voronoi volumes⁵⁴ V_{Voro} and van der Waals volumes V_{vdW} to determine a Voronoi index $V_i = V_{Voro}/V_{vdW}$, a metric indicating the normalised accessible volume for a monomer in the crystal. Voronoi volumes are commonly used to analyse arrangements of molecular condensed phases.^{55,56} V_i values (Figure S1) range from 1.11-1.53, showing that despite the substituent and packing differences, the each monomer in the system has between 10%-50% of its van der Waals volume to freely vibrate, rotate or translate. For the **HC** systems, the average V_i is 1.48, and 1.45 for the **HP** systems. The accessible volume for the **HC** systems shows greater variation but is overall slightly higher than for the less varied **HP** systems. The increased volume for the **HC** systems theoretically allow for greater nuclear relaxation in the excited state. However, reorganisation energies for the **HP** systems are larger than for **HC**, showing the importance of the electronic effects over geometric considerations. In summary, the volume does not seem to be a decisive factor in determining the emissive properties of these systems.

To investigate the intermolecular relationships within the molecular crystals, we examine the topology of the molecular crystals of **HC** and **HP** families by considering dimer packing motifs. Crystal morphologies are commonly described qualitatively as herringbone, face-face, edge-tail, etc. Here we take a more of quantitative approach by constructing maps of each crystal, based on a geometric description of the dimers. These maps allow the topology of the crystal to be analysed graphically, as in Figure 2.

The dimer motifs are quantified through three angle variables, α , β , and γ . These are depicted in Figure 1, and example motifs with associated angles are given in Figure S4. Three axes, x , y , z , are defined on each molecule i and j of the dimer, where x and y are the long and short axes of the molecule, and z is the orthogonal vector. These vectors

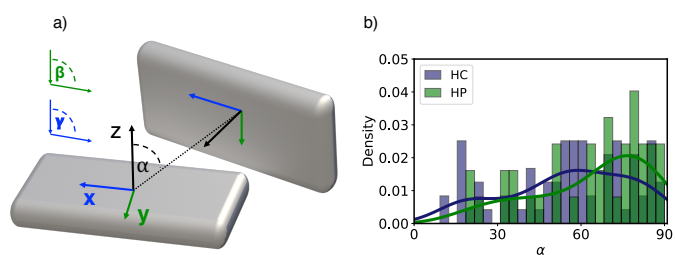


Fig. 1 Panel a), left; schematic of two monomers A and B, their centroids C , and the α , β , and γ angles used to classify dimer configurations. Panel b), right; distribution of α angles for dimers in **HC** and **HP** systems.

comprise an orthogonal basis to describe the dimer. The angles are then defined as:

- α : The azimuthal angle between the monomers as shown in Figure 1. Calculated as the angle between the z -axis located at the centroid of monomer i , and the vector connecting two centroids. α is calculated twice, once with each monomer as the reference. The smallest angle is chosen, provided $0^\circ \leq \alpha \leq 90^\circ$.
- β : The angle between the two short-axis vectors y of each molecule, shown in green in Figure 1. β ranges from 0° to 180° , tracking whether monomers are aligned cofacially parallel ($\beta = 0^\circ$, CoF-P), or cofacially antiparallel ($\beta = 180^\circ$, CoF-A), or in a herringbone edge-face manner (90° , Hb), and all configurations in between. β is commonly described as the “herringbone” angle.
- γ : The angle between the long-axis vectors x , ranging from 0° (parallel, P) to 180° (antiparallel, A). At $\gamma = 90^\circ$, the dimer is T- or L-shaped. The distinction depends on α .

In Figure 1b the distribution density of the α angle is shown for the **HC** and **HP** systems. The distribution is heavily skewed towards 90° , indicating that for the majority of dimers, there is little overlap between the faces of the monomers. As such, it can be expected that in each molecular crystal there are few dimers with the perfect face-face stacking, with most undergoing a displacement in x or y . This is common for aromatic systems.⁵⁷ In particular, we define the x -slip displacement as the distance between molecular centroids along their principal axis. This definition holds for colinear molecules where the principal axes are parallel.

Figure 2 shows the dimer distribution densities for the β and γ angles for **HC** (top row) and **HP** (bottom row). Key regions are highlighted as an example in the upper plot of panel a); for example at $\beta = 90^\circ, \gamma = 0^\circ$, a herringbone (Hb)

stack is witnessed with the long axes arranged in parallel. For both **HC** and **HP** systems, the majority of dimers have β and γ angles close to 180° (top right of plot), indicating that the most common dimer configuration is a cofacial arrangement where the carbonyl groups align antiparallel, at opposing ends of the molecule from each other. This results in an antiparallel alignment of the S_1 transition dipole moment of each monomer.

However, as panel b) shows, when the α angle is used as a filter, the configurations with acute azimuthal angles, and therefore closest in space, are mostly herringbone in nature for **HC**, with carbonyl groups at the same ($\gamma = 0^\circ$) or opposite ends of the dimer ($\gamma = 180^\circ$). In **HC1-3** and **HC6**, the herringbone is the most common dimer, but does not occur at all in the **HP** systems, as shown in Table S2. For example, **HC1** has three herringbone-like dimers and one cofacial dimer. With the largest unit cell and the conformational flexibility of the methoxy group, **HC5** has the greatest variety of dimers, with nine herringbone, ten T-shape, and three cofacial types. In the case of **HC7**, all dimers have a parallel-T shape structure.

The cofacial arrangements favoured by the Kasha model occur at large slip displacements in the x or y plane ($\alpha > 60^\circ$), and are more like edge-edge coplanar arrangements rather than the well-known π -stack. Only in **HC5** is there significant cofacial π -stacking between dimers, with other cofacial arrangements in **HC** and **HP** having larger x -slip. For **HC** compounds, 63% of the cofacially aligned dimers have a x -slip of less than half a molecule, whereas 68% of cofacially-aligned **HP** dimers have a x -slip of more than half a molecule (Figure S2). In particular, the three cofacial dimers of **HC5** have excellent alignment allowing for strong intermolecular interactions, with slip distances of less than half a molecule and all with $\alpha < 40^\circ$.

In the **HP** systems with $\alpha \leq 60^\circ$, configurations lie on the diagonal (Figure 2)b, bottom), indicating dimers centred around a T-shape, which move to L-shaped when $\alpha \geq 60^\circ$. Overall, the significant dimer arrangement in **HP** compounds is a T shape, with the majority of cofacial arrangements having a large x or x -slip with minimal $\pi\pi$ interactions due to the single aryl groups aligning at $y=180^\circ$. The α angle is generally larger than in **HC** with an average of 64° compared to 55° , inhibiting short-range intermolecular interactions. However, in all **HP** systems, there is at least one prominent cofacial dimer which promotes exciton coupling, as we show in the next section.

Our structural analysis shows a significant prevalence of herringbone motifs in the **HC** series, while T-shape motifs are very common in the **HP** series. Nonetheless, the low emitting crystals in the **HC** series (**HC4**, **HC5** and **HC7**) feature a significant population of T-shape motifs like those

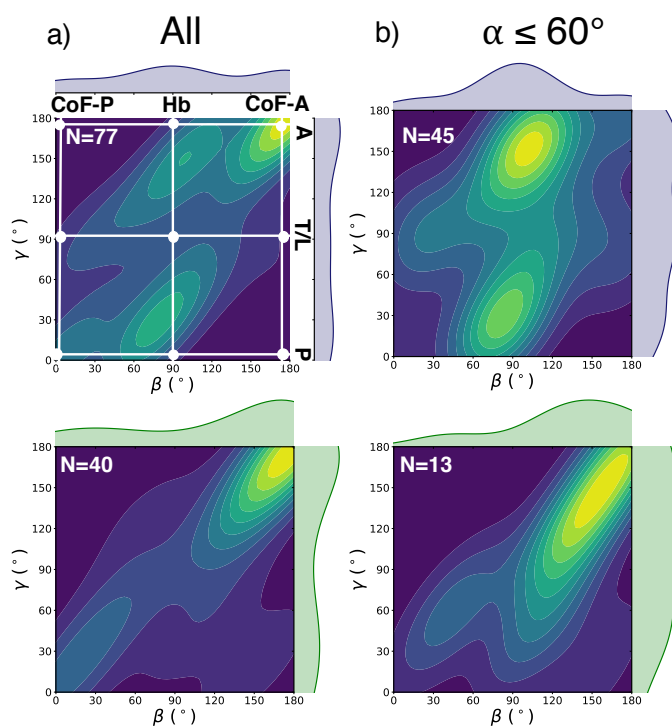


Fig. 2 Panel a), left; Probability density map of the β and γ angles for **HC** (top) and **HP** (bottom) dimers. Key configurations are labelled on the axes, as explained in the text. Panel b), right; probability density for the subset of dimers where $\alpha \leq 60^\circ$.

found in the **HP** crystals. Consequently, the relationship between crystal structure and quantum yield is intertwined with additional factors to such an extent that no general direct rules can be observed.

2.2 Intermolecular interactions in the molecular crystal

Competing with localisation of the excited state necessary for ESIPT is exciton hopping. This competition can delay or even prevent proton transfer.⁵³ Exciton transport can occur through coherent or incoherent hopping between molecular sites, and thus it is important to understand the possible intermolecular transport channels in the **HC** and **HP** systems. For the dimers discussed above, the exciton coupling J_{ij} between monomers i and j is calculated with Troisi's diabatisation scheme based on the orthogonal transformation of adiabatic states to diabatic states.^{58,59} This coupling scheme incorporates both short-range and Coulombic coupling mechanisms. The obtained couplings show a linear correlation with half of the energy splitting between S_1 and S_2 of the dimer (Figure S11).

Considering the close packing of chromophores, we extended this method to assess the effect of a third monomer k on the exciton coupling, where the coupling J_{ij} between

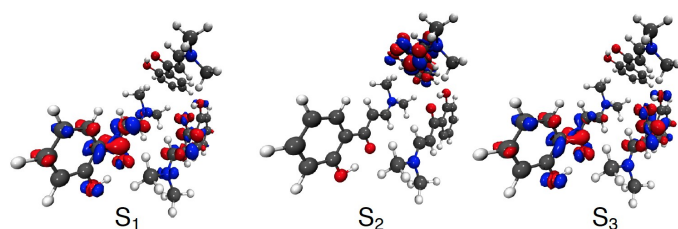


Fig. 3 Electron density difference maps for the first three excited states of the **HP** trimer

monomers i and j incorporates the effect of monomer k , which can be quantified through comparison of the dimeric and trimeric coupling. However, we found that this made very little difference to the coupling in **HC1**, **HC5** and **HP1** compared to the kind of coupling modulations expected due to thermal fluctuations,^{58,60} as reported in Section S4.2. This can be attributed to the excited state being delocalised over no more than two monomers of a trimer (Figure 3, Figures S9 and S10).

Our previous research on the **HC** series showed that the TD- ω B97X-D/6-311++G(d,p) level of theory provides a good representation of the excited state potential energy surfaces of these systems.^{52,53,61} For the **HC** series, the absorption spectra in the solid state show broad bands with maxima in the region of 3.2-3.5 eV, which can be assigned to the absorption of the E form.^{31,51} In the solvents DCM and hexane, the absorption band of **HC1** appears at 2.8 and 3.0 eV respectively. The predicted values in the crystal form are in the range of 3.2-3.4 eV, in very good agreement with the experiments. For the **HP** series, the experimental absorption maximum in DCM is found between 3.4 and 3.5 eV. The experimental absorption maximum of **HP1** in the solid state appears between 3.3 and 3.5 eV,⁵⁰ while the predicted value is blue-shifted (3.8 eV). This level of theory should provide a qualitative understanding of the transport properties of the materials.

The exciton couplings for all dimers and the identity of the dimer with the largest J are shown in Figure 4. In **HC1-4**, where the closest packed dimers are herringbone in nature, the largest coupling occurs in **HC1**, with $J = 108$ meV. For **HC-2**, the dimer with the largest coupling is an edge-edge stacked dimer with $\alpha = 87^\circ$, where poor alignment reduces the coupling to $J = 79$ meV. **HC3** and **HC4** have similar herringbone stacking arrangements, where the largest couplings are 80 meV and 93 meV respectively. In **HC5-7**, face-face stacked dimers are more prevalent in the crystal structure. The size of the coupling in **HC6** is reduced compared to **HC5** due to the y displacement of one of the monomers, with values of 148 meV and 113 meV. A significant drop off to 83 meV is seen for **HC7** due to an increased

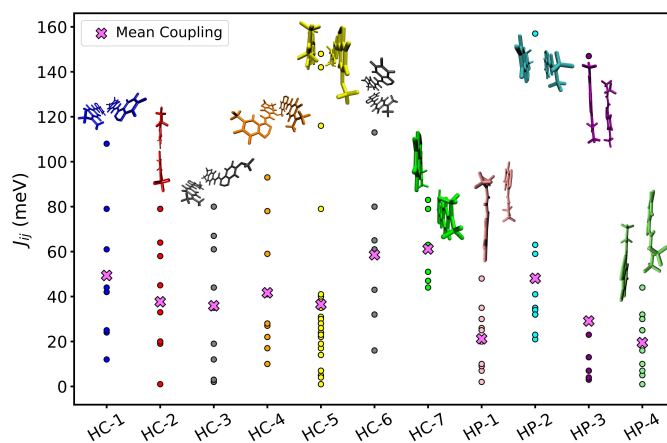


Fig. 4 Exciton couplings J between monomers i and j in the dimers identified in **HC** and **HP**. The mean coupling is also shown.

x -slip in the cofacial dimer.

In the **HP** compounds, the large α and x -slip values, and the smaller molecular size, reduce the average coupling compared to **HC**. In each **HP** derivative there exists one close packed, cofacial dimer which exhibits the largest coupling. For **HP1**, this is relatively small at just 48 meV due to the x -slip. However, in **HP2-3**, the crystal structures afford more efficient cofacial stacking with x -slip values of only 1 Å, resulting in the largest couplings of all investigated systems, with $J = 157$ meV for **HP2** and $J = 147$ meV for **HP3**.

We assign the dimers as H- or J-aggregates based on the oscillator strength of the S_1 and S_2 excitation. In the Kasha model, for a perfectly stacked dimer with no x -slip, the oscillator strength of the S_2 state should be double that of the monomer state. These systems generally fit the Kasha model, as when the x -slip is zero, a linear model (SI section S5) predicts an enhanced S_2 intensity of 2.10 for the **HCs** and 1.83 for the **HPs**. With increasing x -slip, the difference in oscillator strength between the two states decreases until the inversion to J-aggregates is witnessed ($f_{S_1} > f_{S_2}$). For the **HCs** this occurs at a x -slip of 52% of the monomer length and at 46% of the monomer length for the **HCs**.

For almost all systems, the number of H- and J-aggregates is very similar (Table S5). For **HC-4**, **HC-5** and **HC-7** the H-aggregate population grows to 78%, 66% and 100%, respectively. Following Kasha's exciton coupling model, an increase in H-aggregates would be associated with a decrease of the emissive response linked with a smaller radiative rate. However, the QEs are also dependent on nonradiative mechanisms and it has been shown that the prevalence of H dimers does not necessarily mean a low QE.⁶²

2.3 Exciton localisation vs. hopping: the role of nuclear reorganisation and proton transfer

Once the system is in the excited state, relaxation can happen through the K^* or E^* channels (or both). These mechanisms compete with exciton hopping, which prevents localisation of the electron density. For fluorescence to occur from the K^* state, the exciton must localise onto one monomer to enable ESIPT.⁵³ Exciton hopping rates v_{ij} between monomers i and j in a molecular crystal were estimated based on a Marcus hopping scheme,

$$v_{ij} = \frac{J_{ij}^2}{\hbar} \sqrt{\frac{\pi}{\lambda k_B T}} \exp\left[-\frac{\lambda}{4k_B T}\right] \quad (1)$$

where k_B is the Boltzmann constant, \hbar is the reduced Planck constant, T is the temperature (298K), and λ is the reorganisation energy. The activation energy can be approximated as $\lambda/4$.^{63,64} The reorganisation energy λ of Equation 1 is calculated in the adiabatic regime *via*

$$\begin{aligned} \lambda_A &= \lambda_{ex} + \lambda_g \\ &= (E_{ex}^* - E_{ex}) + (E_g^* - E_g) \end{aligned} \quad (2)$$

where E_g and E_{ex} are ground state energies at the S_0 and S_1 minima, and E_g^* and E_{ex}^* are the corresponding excited state energies at respective minima. Herein, we consider the reorganisation energies involved in the relaxation to the K^* and E^* minima (Keto and Enol regimes respectively) within one monomer. λ can also be calculated using normal mode analysis (see SI section S2). However, for **HC1**, **HC5**, and **HP1**, it is found that λ_{NM} overestimates the reorganisation energy with respect to λ_A , so we use λ_A in the following. Herein, our main aim is to provide a qualitative idea of the competition between exciton hopping and proton transfer. The advantages and limitations of this approach are discussed in Ref⁶³.

As discussed previously, the absorption process in these materials is localised over fewer than three monomers at a time. Furthermore, the excited state relaxation channel is confined to one molecule in the S_1 minimum of ESIPT chromophores, and does not involve large rotations of the aromatic rings.^{53,61} This indicates that a large scale reorganisation of the surroundings of the excitation is unlikely, and we can model the radiative process by relaxing one molecule.

Solid state reorganisation energies λ_A in keto and, when located, enol minima were calculated for (TD-) ω B97X-D/6-31G(d):UFF cluster models with a monomer chromophore using Equation 2. Figure 6 shows the coupling, reorganisation energy and the associated exciton hopping rate (using a log scale) for each dimer. The hopping rate v

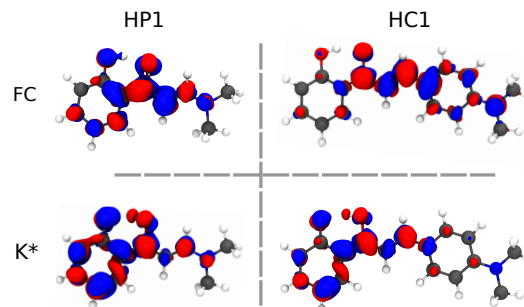


Fig. 5 S_1 - S_0 density profiles for **HP1** and **HC1** in the optimised Frank-Condon and K^* geometries.

is ultrafast in the enol regime (**HC1-4,6,7**), with the highest rates in the region between $1 \times 10^{13} \text{ s}^{-1}$ and $6 \times 10^{13} \text{ s}^{-1}$ due to the planar conformation conferring relatively low λ_A (244 meV on average). The highest and lowest v for **HC1** are $4.18 \times 10^{13} \text{ s}^{-1}$ and $5.17 \times 10^{11} \text{ s}^{-1}$, while the rate of ESIPT in the molecular crystal, through time resolved spectroscopy, is $3 \times 10^{11} \text{ s}^{-1}$.³³ Intermolecular hopping is therefore expected to compete with ESIPT, which requires localisation of the excited state to one site in the molecular crystal. Due to similarity of the electronic and crystal structures, this should also be the case for **HC2-3,6,7**, hence opening nonradiative intermolecular decay channels for these systems and a source of quantum yield leak. For **HC4** and **HC5**, there is a significant bias towards proton transfer because of a larger reorganisation energy (935 meV and 978 meV respectively).

For the **HP** systems, the E^* minima show significant distortion *via* partial trans-cis isomerisation about the aliphatic double bond. For **HP1**, the reorganisation energy associated with the E^* minimum is 2.19 eV. As a direct consequence, the hopping rate for such a large λ is $1.44 \times 10^4 \text{ s}^{-1}$. For comparison, the smallest hopping rate for **HC1** is $5.17 \times 10^{11} \text{ s}^{-1}$.

In summary, for the **HC** systems, reorganisation energies due to ESIPT range from 0.532 eV (**HC3**) to 0.978 eV (**HC5**) compared to 1.06 eV (**HP2**) to 1.23 eV (**HP1**) for **HP**. This is due to the removal of the second aryl group in **HP**, which increases the bias towards ESIPT due to the instability of the planar E^* conformer and the high stability of the K^* conformer.

Consequently, in the K^* channel, hopping rates in the **HPs** are systematically lower than in the **HC** family—on average, $v = 7.51 \times 10^8 \text{ s}^{-1}$ compared to $7.61 \times 10^{10} \text{ s}^{-1}$. The highest rate in the **HP** family is $1.33 \times 10^{10} \text{ s}^{-1}$, compared to a $1.64 \times 10^{12} \text{ s}^{-1}$ in the **HCs**.

The ESIPT bias in **HP** derivatives can be understood through analysis of electronic transition densities, where a loss of electron density at the hydroxyl oxygen increases

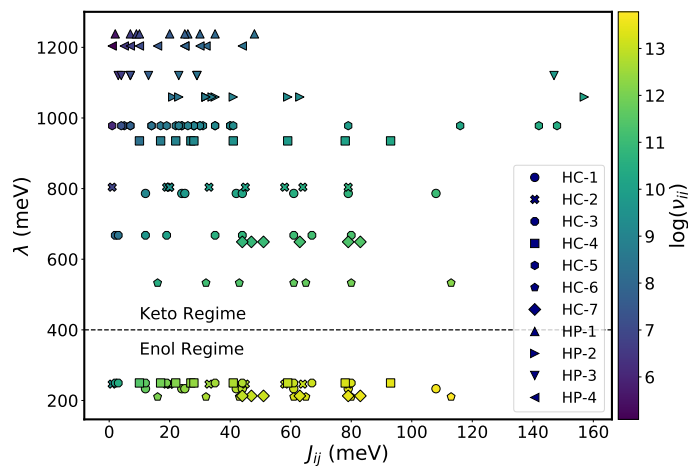


Fig. 6 Colourmap of the exciton hopping rate v_{ij} on a \log_{10} scale, as a function of the exciton coupling J_{ij} and the reorganisation energy λ , calculated via Equation 1.

the acidity of the proton with respect to the **HC** systems, where this loss is not present, except in **HC5**. Figure 5 highlights this for **HP1** and **HC1**. NBO charge analysis of the phenol oxygen shows that Δq increases from +0.01 to +0.05 to +0.09 for **HC1**, **HC5** and **HP1** respectively. This increases the bias for ES IPT in **HC5** and **HP1** due to the increased acidity of the transferring proton, as shown by the excited state PES relaxed geometry scan in Figure S12.

2.4 The Solid State Luminescence Mechanism

The enhancement of luminescence in the condensed phase can be achieved by increasing radiative decay or decreasing the population of nonradiative pathways.²⁴ Both kinds of mechanisms have been considered for ES IPT chromophores in the solid state.^{52,65–67} Herein, we explore in more detail the competition between nonradiative and radiative mechanisms for the **HC1**, **HC5** and **HP1** molecular crystals. For all these crystal, the K^* form is responsible for the emission in the solid state.^{31,51,68} Consequently, our analysis will focus on the mechanisms triggered by the ES IPT.

Reproducing the experimental emission of these systems has proven to be a challenge; our previous work on **HC1** and **HC5** indicated that to obtain emission energies close the experimental values, the S_1 geometry has to be optimised using the crystalline (Ewald) embedding.⁶¹ The fluorescence spectrum was obtained using Ewald embedding and the nuclear ensemble approach.^{69,70} The simulated maxima were 2.1, 2.0 and 2.6 eV for **HC1**, **HC5** and **HP1** respectively, which are in good agreement with the experimental emission maxima at 1.9, 2.0 and 2.3 eV. We estimated the radiative decay rates k_r based on this spec-

trum:

$$k_r = \frac{1}{\hbar} \int \Gamma_r(E) dE \quad (3)$$

where Γ_r is the rate of spontaneous emission per molecule per unit of angular frequency between E/\hbar and $(E + dE)/\hbar$.⁷¹ The spectra for **HC1**, **HC5** and **HP1**, which are the extreme cases, are given in Figure S15 and radiative rates for **HC1**, **HC5** and **HP1** are given in Table 2. The simulated spectra are broader than the experimental ones, which indicates that vibrations of larger amplitude are obtained with the point charge embedding calculation than would be allowed in the solid state environment.

We obtained the experimental k_r rates by evaluating Eq. 3 for the experimental spectra reported in References^{31,51,68}. The k_r rates were also calculated using the experimental excited state lifetimes (τ) of 1.7 and 5.9 ns for **HC5**³³ and **HP1**⁵⁰ and the experimental quantum yields $k_r = \frac{\Phi}{\tau}$. We estimated the nonradiative decay rates, using the experimental quantum yields, as $k_{nr} = k_r \frac{1-\Phi}{\Phi}$.

While the values obtained from different experimental techniques differ, they possess some common qualitative features. The radiative decay constants for the three systems are of the same order of magnitude. Consequently, the different emissive behaviour cannot be explained by only considering radiative mechanisms. The calculated values of k_{nr} based on the experimental QEs are $1.3 \times 10^8 \text{ s}^{-1}$, $7.1 \times 10^9 \text{ s}^{-1}$ and $2.4 \times 10^7 \text{ s}^{-1}$ for **HC1**, **HC5** and **HP1** respectively. In the weak electronic coupling regime, nonradiative decay can occur because of the overlap of vibrational states.⁷² The RIM model addresses this extreme case.

According to the RIM interpretation, the switch-on of fluorescence in the condensed phase is due to dampening of low energy vibrational modes, which dissipate the excited state nonradiatively, as witnessed by a reduction in the HR factors. While **HC1**, **HC5** and **HP1** show a significant decrease of the contribution of low frequency modes to the reorganisation energies in the solid state, **HC5** is dark in both dispersed and aggregated forms, in contrast with **HC1** and **HP1**.^{31,68} This shows that dampening of low energy vibrational modes, in-plane and out-of-plane intramolecular rotations, is not a sufficient condition to explain the enhancement of emission in the condensed phase (Figure 7 and Section S2 in the SI). This indicates that nonradiative decay occurs in the strong electronic coupling regime, consequently, nonradiative decay should involve conical intersections.⁵³

We have shown that for **HC1**, fluorescence is possible due to the high energy conical intersection in the solid state. On the other hand, for **HC5** and **HC4**, whilst ES IPT is more efficient than in **HC1**, the QE is very small.⁴⁹

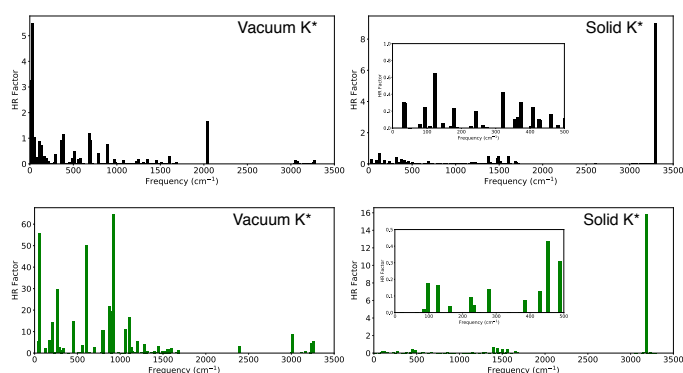


Fig. 7 Huang-Rhys factors associated with each normal mode calculated *via* the Duschinsky rotation matrix between K^* and S_0 electronic states for **HC5** (Black) and **HP1** (Green). Frequencies 0-500 cm^{-1} in the solid state are shown in the inset.

Table 2 Radiative decay rates k_r in the solid state in the enol (E^*) and keto (K^*) regimes for **HC1**, **HC5**, **HP1**. All rates in s^{-1} .

System	k_r^{Exp}	k_r	k_{nr}^{Exp}	k_{nr}
HC1	3.1×10^7 (2.0×10^8)	6.7×10^7	6.0×10^7 (3.9×10^8)	1.3×10^8
HC5	4.7×10^7	7.2×10^7	4.7×10^9	7.1×10^9
HP1	4.8×10^7 (1.3×10^8)	6.7×10^7	1.7×10^7 (4.5×10^7)	2.4×10^7

This can be attributed to dominance of nonradiative decay as a result of a low-lying MECI being classically accessible post electronic excitation.^{52,53} While intermolecular factors play a role in the conformation of the MECI, the energetic accessibility is determined by the electronic structure of the chromophore. To assess the accessibility of the MECI in the solid-state in **HP1**, we construct the excitation-decay pathway in the using QM:MM cluster models. The calculated PES for **HP1** in vacuum and the solid state is shown in Figure 8.

At the MS-3-CASPT2(12,11)/6-31G(d):AMBER level, absorption for **HP1** is calculated at 3.67 eV ($f=0.868$), in fair agreement but blue-shifted by 0.41 eV compared with the crystalline absorption maximum of 3.26 eV.⁵⁰ Post photo-excitation, relaxation in S_1 *via* ESIPT is expected to be the dominant relaxation channel in **HP1** due to the negligible oscillator strength ($f=0.016$) of the S_2 state, which is $n\pi^*$ in character. Fluorescence in the molecular crystal is centred at 2.34 eV, thus displaying a Stokes shift of 0.94 eV. The emission wavelength predicted at CASPT2 is 2.73 eV, again in fair agreement and with similar blue-shift as calculated for absorption.

The MECI in **HP1** lies 1.46 eV above the K^* minimum and 1.08 eV above the bright absorption state. As such, it is classically inaccessible and **HP** emission can be attributed

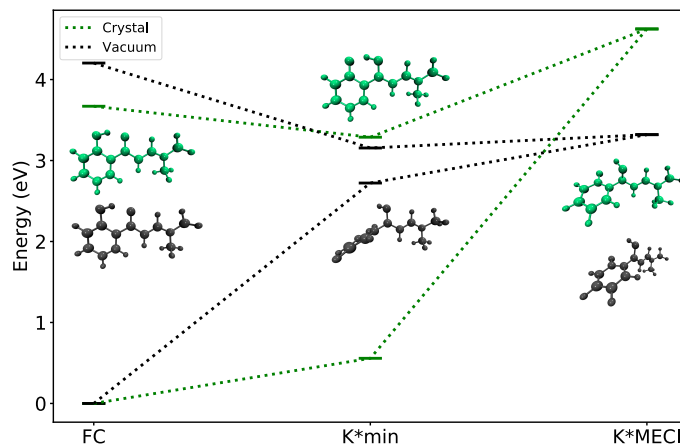


Fig. 8 Calculated energies and geometries at critical points on PES. Crystal geometries obtained with ONIOM((TD)- ω B97X-D/6-31G(d):AMBER), with energies calculated at MS-3-CASPT2(12,11):AMBER. Vacuum geometries obtained with (TD)- ω B97X-D/6-311++G(d,p) and energies obtained with MS-3-CASPT2(12,11). The average energy of the S_1 and S_0 states is shown for the MECI.

to the trapping of the excited state at the K^* minimum, followed by radiative decay. As the substituent effects in the crystalline samples are minor in the **HP** samples, it can be assumed that this mechanism can be applied to all four systems in the family. It would be of interest to synthesise a **HP** system to assess its AIE behaviour with a methoxy group the *para* position, as in **HC5**.

In Figure 9, the solid state MECI geometries of **HC1**, **HC5**, and **HP1** are compared. All three involve the pyramidalisation of the protonated carbonyl group combined with torsional rotation of the deprotonated phenol moiety. The lowest energy conical intersections in vacuum, which only involve torsional rotation, are restricted in the solid state. In **HC1** and **HP1**, the compounds which undergo SLE due to the high energy of the MECI, the torsional angles are 49.6° and 53.3° . In **HC5**, where the MECI is energetically accessible, the pyramidal distortion is only 26.7° . The same effect is seen in vacuum, where the MECI of **HC5** is also onset at lesser distortion than the other systems, as discussed above and shown in Figure S13. The high energy MECIs of **HC1** and **HP1**, are inherent to the electronic effects of the chromophore and the restriction of large amplitude motions in the crystal environment. Crystal packing as a whole promotes efficient localisation of the excited state at the expense of exciton hopping in the enol state. A largely increased QE is witnessed as a result of the high propensity for ESIPT in **HP** and the high energy of the conical intersection.

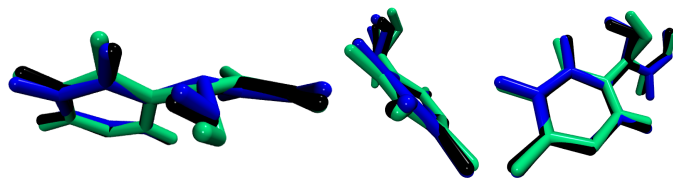


Fig. 9 Overlaid structures of the MECI for **HC1** (blue) and **HC5** (black), and **HP1** (green), shown from three viewpoints. Only the atoms shared by all three compounds are shown.

3 Conclusions

In this work we have systematically evaluated the photo behaviour of a range of solid-state emitters based on the ESIPT mechanism. In the **HC** family of compounds, AIE is witnessed for five of the seven compounds, with QEs ranging from 0.1 to 0.41. In the **HP** systems, which differ by containing only one aryl ring, all reported compounds are emissive in the solid state with QEs of 0.72-0.84. In each crystal structure, there exist a range of dimer motifs each with their own excitonic profile. There are no direct structure-property relations that correlate the prevalence of certain structural patterns and quantum yields. While herringbone motifs are commonly found in the emissive **HC** crystals and the those with lower quantum efficiencies have a significant population of T-shape motifs, the completely emissive **HP** series also exhibits the latter conformations.

In the **HC** compounds (except **HC4** and **HC5**) after photoexcitation to the S_1 state, exciton hopping in the enol tautomer will compete with ESIPT on account of minimal electron density loss on the phenol oxygen and the stability of the planar enol tautomer, which results in only a small reorganisation energy. Here the hopping rate is several orders of magnitude larger than in the K^* state and will allow nonradiative dissipation of the excited state. Conversely in the **HP** compounds, **HC4**, and **HC5**, the electron density loss is increased on the oxygen and ESIPT is more favourable, coupled with the planar E^* tautomer being unstable. The stability of the K^* state increases the reorganisation energy λ of the chromophore and subsequently will increase the population of the ESIPT channel in these systems. The K^* state will be highly localised with minimal electron hopping.

The K^* minimum takes a planar conformation in the solid state, with considerable oscillator strength for emission. **HP1** has an energetically inaccessible MECI, like **HC1**, whereas in **HC5** the MECI is energetically accessible. As for **HC1**, the MECI for **HP1** in the crystal takes a distorted, pyramidalised geometry and is energetically inaccessible in the decay path. As such, emission will occur from the planar K^* minimum for the **HP** compounds and

with larger QE, due to the increase in the population of the K^* channel. Such is the similarity in absorption and emission spectra across the **HP** family, this mechanism is expected to be independent of the substituents present in this study.

Exciton hopping is reduced in series **HP** due to the relatively small exciton coupling and the bias for ESIPT on account of the electron density redistribution, rendering ESIPT the most favourable relaxation channel in the solid state. The competition between delocalisation and localisation could play a role in the case of certain of the molecules of the **HC** series (**HC1-3** and **HC6-7**).

At this point, we can say that the incorporation of the following features into the next generation of ESIPT emitters can move the field forward, based on the remarkable properties of the **HP** derivatives:

1. To maximise the population of the ESIPT channel, chromophore design should encourage a highly labile proton, where electronic excitation destabilises the E^* state.
2. Packing modes should limit π - π interactions, which enable exciton coupling and delocalisation. However, if the ESIPT is favourable enough, the localisation inherent to the K^* state can overcome unfavourable stacking arrangements.
3. In the K^* form, solid state conical intersections are accessed *via* a combination of pyramidalisation and rotation. This can be made more unfavourable by tethering and chromophore design, where we have shown that simple measures such as scanning coordinates in vacuum can predict K^* stability.

This work connects the electronic, molecular picture with the crystalline regime for organic, light-emitting materials. The deconstruction of intra- and intermolecular factors here, connecting the chromophore with its crystal structure, offers a step forward in first principles design of solid state luminescent materials.

4 Computational Methods

The crystal structures of compounds **HC1-7** and **HP1-4** were obtained from the CCDC as described in references 49–51. Monomers of **HC1-5** and **HP1-4** were optimised in vacuum in the S_0 and S_1 enol and keto states at the (TD)- ω B97X-D/6-311++G(d,p) level of theory. Relaxed geometry scans of the torsional rotation angle in the keto S_1 state (K^*) were performed for the same compounds. Proton migration scans of the ESIPT process were also performed in vacuum for **HC1** and **HP1**. All scans were calculated with TD- ω B97X-D/6-31G(d).

The crystal structures of all **HC** and **HP** compounds were optimised using Quantum Espresso in the periodic DFT framework.⁷³ Optimisation of each unit cell was carried out with DFT-D2 (PBE) with a plane-wave cutoff of 30 Ry and ensuring Monkhorst-Pack k-point convergence in each case.

Exciton couplings J_{ij} were calculated for dimers in each optimised crystal structure. A 2x2x2 supercell was constructed for each system, starting from the optimised unit cell, and all unique dimers were identified and extracted. A dimer was defined as any molecular pair with an interatomic distance less than or equal to the van der Waals radii of the atoms plus a distance of 1.5Å. This selection criterion has previously been used in similar applications.⁷⁴ The coupling J_{ij} between monomers i and j in unique dimers are calculated in Troisi's diabaticization scheme based on the orthogonal transformation of adiabatic states to diabatic states using the transition dipole moments.^{58,59} Further details are given in Section S4.

Crystalline emission spectra for **HC1**, **HC5** and **HP1** in E* and K* minima were simulated using the nuclear ensemble method as implemented in the NEWTON-X software suite.⁶⁹ 2000 initial conditions were sampled from the harmonic frequencies calculated with QM:QM' ONIOM(TD- ω B97X-D/6-311++G(d,p):HF/STO-3G) using the Ewald Embedded Cluster model (EEC).⁶¹ The S₁-S₀ energy gap was computed for each initial condition in embedded point charges to reflect the positions of the surrounding crystal atoms. No QM'-level energies were computed, and as such the fluorescence spectra are of only the electronic energies.

To calculate solid state reorganisation energies in the adiabatic approximation (λ_A), for each compound we generated cluster models based on the 2x2x2 supercell, where all molecules which lay within 20Å of the central chromophore were included in the cluster. Geometries were optimised in S₁ and S₀ states within the ONIOM protocol at ω B97X-D/6-31G(d):UFF using electronic embedding. MM charges were derived automatically using the QEq method.⁷⁵ The UFF forcefield was chosen here due to the automatic charge assignment, allowing the high-throughput generation of structures and input files. In the cases of **HC1-4** and **HC6-7**, λ_A was calculated for both the enol and keto pathways. For **HC5** and **HP1-4**, only the λ_A associated with keto relaxation was used since no E* minimum was located in the monomer QM:MM relaxation.

For **HC1**, **HC5**, and **HP1**, additional ONIOM calculations were carried out with ONIOM(TD- ω B97X-D/6-311++G(d,p):HF/STO-3G) using EEC and 7Å clusters. Here, the embedding charges came from RESP calculations at TD- ω B97X-D/6-311++G(d,p) level and extend beyond the nearest neighbour molecule, reaching 10,000

point charges at lattice positions which are additionally fitted to match the exact Ewald potential of the crystal.^{76,77} `fromage` was used to optimise geometries and to provide an interface between different electronic structure codes.⁶¹

Reorganisation energies in the normal-mode approximation (λ_{NM}) were calculated using the DUSHIN program for **HC1**, **HC5** and **HP1**.⁷⁸ Frequencies for an ONIOM-optimised monomer chromophore were calculated in an array of point charges representing the molecular crystal, at TD- ω B97X-D/6-31G(d) level. This led to one imaginary frequency in each case.

The radiative rates k_r in the molecular crystals of **HC1**, **HC5**, and **HP1** were calculated by simulating the fluorescence spectrum using the nuclear ensemble method.⁷⁰ Excited state frequencies at the K* minimum for a monomer chromophore were calculated at ONIOM(TD- ω B97X-D/6-311++G(d,p):HF/STO-3G) level of theory and used to generate 2000 initial conditions using a Wigner distribution. For each initial condition the S₁-S₀ energy gap was calculated in a bed of point charges representing the crystal atoms at TD- ω B97X-D/6-311++G(d,p) level of theory. Integration of the spectrum gives k_r as described in reference 70.

For **HP1**, the full excited state decay mechanism was established through QM:MM cluster models using density functional and multireference methods. A monomer and trimer chromophore at the centroid of the 20Å cluster were optimised in the ground and excited states at (TD-) ω B97X-D/6-31G(d):AMBER level of theory. The S₁/S₀ MECI in both monomer and trimer cluster models were calculated using a modified version of the CIOpt algorithm.^{79,80}

The MECI in the monomer cluster models was also obtained with the state-averaged complete active space self-consistent field method, employing the S₀ and S₁ states in the averaging. The active space consisted of 12 electrons in 11 orbitals (SA-2-CASSCF(12,11)), shown in Figure S11. The 6-31G(d) basis set was used for the QM region and the AMBER forcefield was used to describe the MM region. Calculating the MECI with CASSCF:MM ensures the validity of the TD-DFT:MM-calculated MECI. The potential energy profile was refined with multistate complete active space second-order perturbation theory (MS-3-CASPT2(12,11)/6-31G(d):AMBER), incorporating the S₀, S₁, and S₂ states. The TD-DFT:MM geometries from the trimer models at the Franck-Condon, S₁ minimum, and MECI were taken as the reference geometries, where the central molecule was taken for the CASPT2 calculation and the remaining two molecules of the trimer were added to the MM region. A three state average was used due to include the S₂ electronic state at the Franck-Condon geometry. The orbitals chosen for the active space are shown in

Figure S11. All density functional calculations were performed in the Gaussian 09 suite of programs.⁸¹ CASSCF and CASPT2 calculations used OpenMolcas with the Tinker v.6.3.3 interface.⁸²

To analyse the spatial environment for the monomers at the centre of the cluster models in the each crystal, Voronoi cells partition the crystal into molecular regions. These cells define all the points in space which are closer to the reference molecule than an exterior molecule. Dividing the Voronoi cell volume by the van der Waals volume gives a molecule-independent Voronoi index V_i for each crystal structure. To generate the Voronoi cells, a cluster of molecules was extracted from its crystalline positions. A real space grid was generated at an arbitrary resolution and at each point of this grid, the distance to each atom was calculated and scaled by the corresponding van der Waals radius. All voxels with the lowest scaled distance belonging to an atom of the central molecule were marked as belonging to the accessible of the molecule, resulting in an irregular polyhedron of finite volume. The analysis of volumes and dimer motifs is implemented in the package fromage.⁸³

Acknowledgements

This work was supported by the EPSRC (EP/R029385/1). This research utilized Queen Mary's Apocrita HPC facility, supported by QMUL Research-IT, ARCHER UK National Supercomputing Service (EP/L000202/1) via the Materials Chemistry Consortium and the Molecular Modelling Hub for computational resources, MMM Hub, which is partially funded by EPSRC (EP/P020194/1). The authors thank Jeff Reimers for supplying the DUSHIN code. The authors acknowledge the support from the School of Biological and Chemical Sciences at Queen Mary University of London.

References

- 1 P. I. Shih, C. Y. Chuang, C. H. Chien, E. W. G. Diao and C. F. Shu, *Adv. Funct. Mater.*, 2007, **17**, 3141–3146.
- 2 J. Huang, N. Sun, Y. Dong, R. Tang, P. Lu, P. Cai, Q. Li, D. Ma, J. Qin and Z. Li, *Adv. Funct. Mater.*, 2013, **23**, 2329–2337.
- 3 Z. Zhao, Z. Li, J. W. Y. Lam, J.-L. Maldonado, G. Ramos-Ortiz, Y. Liu, W. Yuan, J. Xu, Q. Miao and B. Z. Tang, *Chem. Commun.*, 2011, **47**, 6924.
- 4 M. P. Aldred, G.-F. Zhang, C. Li, G. Chen, T. Chen and M.-Q. Zhu, *J. Mater. Chem. C*, 2013, **1**, 6709.
- 5 Y. Li, L. Xu and B. Su, *Chem. Commun.*, 2012, **48**, 4109–4111.
- 6 R. T. K. Kwok, C. W. T. Leung and W. Y. Lam, *Chem. Soc. Rev.*, 2015, **44**, 4228–4238.

- 7 J. Gierschner and S. Y. Park, *J. Mater. Chem. C*, 2013, **1**, 5818.
- 8 J. Mei, N. L. C. Leung, R. T. K. Kwok, J. W. Y. Lam and B. Z. Tang, *Chem. Rev.*, 2015, **115**, 11718–11940.
- 9 J. Mei, Y. Hong, J. W. Y. Lam, A. Qin, Y. Tang and B. Z. Tang, *Adv. Mater.*, 2014, **26**, 5429–5479.
- 10 J. Gierschner, L. Lüer, B. Milián-Medina, D. Oelkrug and H. J. Egelhaaf, *Journal of Physical Chemistry Letters*, 2013, **4**, 2686–2697.
- 11 H. Qian, M. E. Cousins, E. H. Horak, A. Wakefield, M. D. Liptak and I. Aprahamian, *Nature Chemistry*, 2017, **9**, 83–87.
- 12 B. K. An, S. K. Kwon, S. D. Jung and S. Y. Park, *Journal of the American Chemical Society*, 2002, **124**, 14410–14415.
- 13 A. Prlj, N. Došlić and C. Corminboeuf, *Phys. Chem. Chem. Phys.*, 2016, **18**, 11606–11609.
- 14 Y. J. Gao, X. P. Chang, X. Y. Liu, Q. S. Li, G. Cui and W. Thiel, *J. Phys. Chem. A*, 2017, **121**, 2572–2579.
- 15 X.-L. Peng, S. Ruiz-Barragan, Z.-S. Li, Q.-S. Li and L. Blancafort, *J. Mater. Chem. C*, 2016, **4**, 2802–2810.
- 16 Q. Li and L. Blancafort, *Chem. Commun.*, 2013, **49**, 5966–5968.
- 17 W. Li, L. Zhu, Q. Shi, J. Ren, Q. Peng and Z. Shuai, *Chem. Phys. Lett.*, 2017, **683**, 507–514.
- 18 X. Zheng, Q. Peng, L. Zhu, Y. Xie, X. Huang and Z. Shuai, *Nanoscale*, 2016, **8**, 15173–15180.
- 19 T. Zhang, Q. Peng, C. Quan, H. Nie, Y. Niu, Y. Xie, Z. Zhao, B. Z. Tang and Z. Shuai, *Chem. Sci.*, 2016, **7**, 5573–5580.
- 20 T. Zhang, H. Ma, Y. Niu, W. Li, D. Wang, Q. Peng, Z. Shuai and W. Z. Liang, *Journal of Physical Chemistry C*, 2015, **119**, 5040–5047.
- 21 T. Zhang, Y. Jiang, Y. Niu, D. Wang, Q. Peng and Z. Shuai, *Journal of Physical Chemistry A*, 2014, **118**, 9094–9104.
- 22 Q. Wu, T. Zhang, Q. Peng, D. Wang and Z. Shuai, *Physical Chemistry Chemical Physics*, 2014, **16**, 5545–52.
- 23 Q. Wu, Q. Peng, Y. Niu, X. Gao and Z. Shuai, *Journal of Physical Chemistry A*, 2012, **116**, 3881–3888.
- 24 R. Crespo-Otero, Q. Li and L. Blancafort, *Chem. Asian J.*, 2019, **14**, 700–714.
- 25 J. Shi, L. E. Aguilar Suarez, S. J. Yoon, S. Varghese, C. Serpa, S. Y. Park, L. Lüer, D. Roca-Sanjuán, B. Milián-Medina and J. Gierschner, *Journal of Physical Chemistry C*, 2017, **121**, 23166–23183.
- 26 J. Gierschner, Y. S. Huang, B. Van Averbeke, J. Cornil, R. H. Friend and D. Beljonne, *Journal of Chemical Physics*, 2009, **130**, year.

- 27 N. J. Hestand and F. C. Spano, *Accounts of Chemical Research*, 2017, **50**, 341–350.
- 28 T. N. V. Karsili, B. Marchetti and M. N. R. Ashfold, *Dalton Trans.*, 2016, **45**, 18921–18930.
- 29 C. Azarias, Á. Budzák, A. D. Laurent, G. Ulrich and D. Jacquemin, *Chem. Sci.*, 2016, **7**, 3793–3774.
- 30 D. Ghosh, G. Ahamed, S. Batuta, N. A. Begum and D. Mandal, *J. Phys. Chem. A*, 2016, **120**, 44–54.
- 31 J. Cheng, D. Liu, W. Li, L. Bao and K. Han, *J. Phys. Chem. C*, 2015, **119**, 4242–4251.
- 32 L. A. Baker, M. D. Horbury, S. E. Greenough, P. M. Coulter, T. N. V. Karsili, G. M. Roberts, A. J. Orr-Ewing, M. N. R. Ashfold and V. G. Stavros, *J. Phys. Chem. Lett.*, 2015, **6**, 1363–1368.
- 33 N. I. Zahid, M. S. Mahmood, B. Subramanian, S. Mohd Said and O. K. Abou-Zied, *J. Phys. Chem. Lett.*, 2017, 5603–5608.
- 34 H. Song, Z. Kuang, X. Wang, Y. Guo, Q. Guo, H. Zhang and A. Xia, *J. Phys. Chem. C*, 2018, **122**, 15108–15117.
- 35 Y. Shinozaki, M. Yamaji and T. Arai, *J. Photochem. Photobiol., A.*, 2018, **350**, 17–22.
- 36 I. E. Serdiuk, M. Wera and A. D. Roshal, *J. Phys. Chem. A*, 2018, acs.jpca.7b10361.
- 37 R. Li, L. Yan, Z. Wang and Z. Qi, *Journal of Molecular Structure*, 2017, **1136**, 1–6.
- 38 J. Li, Y. Wu, Z. Xu, Q. Liao, H. Zhang, Y. Zhang, L. Xiao, J. Yao and H. Fu, *J. Mater. Chem. C*, 2017, **5**, 12235–12240.
- 39 X. Cheng, F. Li, S. Han, Y. Zhang, C. Jiao, J. Wei, K. Ye, Y. Wang and H. Zhang, *Sci. Rep.*, 2015, **5**, 9140.
- 40 T. Teshima, M. Takeishi and T. Arai, *New J. Chem.*, 2009, **33**, 1393.
- 41 Y. Norikane, H. Itoh and T. Arai, *J. Phys. Chem. A*, 2002, **106**, 2766–2776.
- 42 Y. Norikane, N. Nakayama, N. Tamaoki, T. Arai and U. Nagashima, *J. Phys. Chem. A*, 2003, **107**, 8659–8664.
- 43 P.-t. Chou, M. L. Martinez and W. C. Cooper, *J. Am. Chem. Soc.*, 1992, **114**, 4943–4944.
- 44 T. Arai and Y. Norikane, *Direct Observation of the Photoinduced Hydrogen Atom Transfer in 2'-Hydroxychalcone*, 1997.
- 45 X. Jin, L. Dong, X. Di, H. Huang, J. Liu, X. Sun, X. Zhang and H. Zhu, *RSC Adv.*, 2015, **5**, 87306–87310.
- 46 Z. Song, R. T. K. Kwok, E. Zhao, Z. He, Y. Hong, J. W. Y. Lam, B. Liu and B. Z. Tang, *ACS Appl. Mater. Interfaces*, 2014, **6**, 17245–54.
- 47 Y. Pil Kim, H. Seung Ban, S. Sung Lim, N. Kimura, S. Hoon Jung, J. Ji, S. Lee, N. Ryu, S. Rok Keum, K. Hyun Shin and K. Ohuchi, *J. Pharm. Pharmacol.*, 2001, **53**, 1295–1302.
- 48 P. Singh, A. Anand and V. Kumar, *Eur. J. Med. Chem.*, 2014, **85**, 758–777.
- 49 X. Cheng, K. Wang, S. Huang, H. Zhang, H. Zhang and Y. Wang, *Angew. Chem., Int. Ed.*, 2015, **54**, 8369–8373.
- 50 B. Tang, H. Liu, F. Li, Y. Wang and H. Zhang, *Chem. Commun.*, 2016, **52**, 6577–6580.
- 51 X. Cheng, Y. Zhang, S. Han, F. Li, H. Zhang and Y. Wang, *Chem. Eur. J.*, 2016, **22**, 4899–4903.
- 52 M. Dommett and R. Crespo-Otero, *Phys. Chem. Chem. Phys.*, 2017, **19**, 2409–2416.
- 53 M. Dommett, M. Rivera and R. Crespo-Otero, *J. Phys. Chem. Lett.*, 2017, **8**, 6148–6153.
- 54 G. Voronoi, *J. Reine Angew. Math.*, 1907, **133**, 97–178.
- 55 P. Procacci and R. Scateni, *Int. J. Quantum Chem.*, 1992, **42**, 1515–1528.
- 56 J. S. Hunjan and B. C. Eu, *J. Chem. Phys.*, 2010, **132**, year.
- 57 C. R. Martinez and B. L. Iverson, *Chem. Sci.*, 2012, **3**, 2191–2201.
- 58 J. Aragón and A. Troisi, *Phys. Rev. Lett.*, 2015, **114**, 1–5.
- 59 R. P. Fornari, J. Aragón and A. Troisi, *J. Phys. Chem. C*, 2016, **120**, 7987–7996.
- 60 J. Aragón and A. Troisi, *Adv. Funct. Mater.*, 2016, **26**, 2316–2325.
- 61 M. Rivera, M. Dommett and R. Crespo-Otero, *J. Chem. Theory Comput.*, 2019, **15**, 2504–2516.
- 62 J. Gierschner, S. Varghese and S. Y. Park, *Advanced Optical Materials*, 2016, **4**, 348–364.
- 63 V. Stehr, R. F. Fink, B. Engels, J. Pflaum and C. Deibel, *J. Chem. Theory Comput.*, 2014, **10**, 1242–1255.
- 64 A. Kimura, T. Kakitani and T. Yamato, *The Journal of Physical Chemistry B*, 2000, **104**, 9276–9287.
- 65 D. Presti, F. Labat, A. Pedone, M. J. Frisch, H. P. Hratchian, I. Ciofini, M. C. Menziani and C. Adamo, *Journal of Chemical Theory and Computation*, 2014, **10**, 5577–5585.
- 66 D. Presti, L. Wilbraham, C. Targa, F. Labat, A. Pedone, M. C. Menziani, I. Ciofini and C. Adamo, *J. Phys. Chem. C*, 2017, **121**, 5747–5752.
- 67 S. Park, J. E. Kwon, S.-Y. Park, O.-H. Kwon, J. K. Kim, S.-J. Yoon, J. W. Chung, D. R. Whang, S. K. Park, D. K. Lee, D.-J. Jang, J. Gierschner and S. Y. Park, *Advanced Optical Materials*, 2017, **5**, 1700353.
- 68 B. Tang, C. Wang, Y. Wang and H. Zhang, *Angewandte Chemie - International Edition*, 2017, **56**, 12543–12547.
- 69 M. Barbatti, M. Ruckebauer, F. Plasser, J. Pittner, G. Granucci, M. Persico and H. Lischka, *Wiley Interdis-*

- cip. Rev. Comput. Mol. Sci.*, 2014, **4**, 26–33.
- 70 R. Crespo-Otero and M. Barbatti, *Theor. Chem. Acc.*, 2012, **131**, 1–14.
- 71 Y. Niu, Q. Peng, C. Deng, X. Gao and Z. Shuai, *J. Phys. Chem. A*, 2010, **114**, 7817–7831.
- 72 D. Escudero, 2019, **29**, 259–288.
- 73 P. Giannozzi, S. Baroni, N. Bonini, M. Calandra, R. Car, C. Cavazzoni, D. Ceresoli, G. L. Chiarotti, M. Cococcioni, I. Dabo, A. Dal Corso, S. de Gironcoli, S. Fabris, G. Fratesi, R. Gebauer, U. Gerstmann, C. Gougousis, A. Kokalj, M. Lazzeri, L. Martin-Samos, N. Marzari, F. Mauri, R. Mazzarello, S. Paolini, A. Pasquarello, L. Paulatto, C. Sbraccia, S. Scandolo, G. Sclauzero, A. P. Seitsonen, A. Smogunov, P. Umari and R. M. Wentzcovitch, *J. Phys. Condens. Matter*, 2009, **21**, 395502.
- 74 J. E. Campbell, J. Yang and G. M. Day, *J. Mater. Chem. C*, 2017, **5**, 7574–7584.
- 75 A. K. Rappé, L. M. Bormann-Rochotte, D. C. Wiser, J. R. Hart, M. A. Pietsch, C. J. Casewit and W. M. Skiff, *Mol. Phys.*, 2007, **105**, 301–324.
- 76 S. E. Derenzo, M. K. Klintonberg and M. J. Weber, *J. Chem. Phys.*, 2000, **112**, 2074–2081.
- 77 M. Klintonberg, S. Derenzo and M. Weber, *Comput. Phys. Commun.*, 2000, **131**, 120–128.
- 78 J. R. Reimers, *J. Chem. Phys.*, 2001, **115**, 9103–9109.
- 79 B. G. Levine, J. D. Coe and T. J. Martínez, *J. Phys. Chem. B*, 2008, **112**, 405–413.
- 80 R. Crespo-Otero, N. Kungwan and M. Barbatti, *Chem. Sci.*, 2015, **6**, 5762–5767.
- 81 M. J. Frisch, G. W. Trucks, H. B. Schlegel, G. E. Scuseria, M. A. Robb, J. R. Cheeseman, G. Scalmani, V. Barone, B. Mennucci, G. A. Petersson, H. Nakatsuji, M. Caricato, X. Li, H. P. Hratchian, A. F. Izmaylov, J. Bloino, G. Zheng, J. L. Sonnenberg, M. Hada, M. Ehara, K. Toyota, R. Fukuda, J. Hasegawa, M. Ishida, T. Nakajima, Y. Honda, O. Kitao, H. Nakai, T. Vreven, J. A. Montgomery, J. E. Peralta, F. Ogliaro, M. Bearpark, J. J. Heyd, E. Brothers, K. N. Kudin, V. N. Staroverov, R. Kobayashi, J. Normand, K. Raghavachari, A. Rendell, J. C. Burant, S. S. Iyengar, J. Tomasi, M. Cossi, N. Rega, J. M. Millam, M. Klene, J. E. Knox, J. B. Cross, V. Bakken, C. Adamo, J. Jaramillo, R. Gomperts, R. E. Stratmann, O. Yazyev, A. J. Austin, R. Cammi, C. Pomelli, J. W. Ochterski, R. L. Martin, K. Morokuma, V. G. Zakrzewski, G. A. Voth, P. Salvador, J. J. Dannenberg, S. Dapprich, A. D. Daniels, Farkas, J. B. Foresman, J. V. Ortiz, J. Cioslowski and D. J. Fox, *Gaussian 09, Revision D.01*, 2009.
- 82 F. Aquilante, J. Autschbach, R. K. Carlson, L. F. Chibotaru, M. G. Delcey, L. De Vico, I. Fdez Galván, N. Ferré, L. M. Frutos, L. Gagliardi, M. Garavelli, A. Giussani, C. E. Hoyer, G. Li Manni, H. Lischka, D. Ma, P. Å. Malmqvist, T. Müller, A. Nenov, M. Olivucci, T. B. Pedersen, D. Peng, F. Plasser, B. Pritchard, M. Reiher, I. Rivalta, I. Schapiro, J. Segarra-Martí, M. Stenrup, D. G. Truhlar, L. Ungur, A. Valentini, S. Vancoillie, V. Veryazov, V. P. Vysotskiy, O. Weingart, F. Zapata and R. Lindh, *J. Comput. Chem.*, 2016, **37**, 506–541.
- 83 M. Rivera, M. Dommett, A. Sidat, W. Rahim and R. Crespo Otero, *ChemRxiv*, 2019.